Available online at www.sciencedirect.com

ScienceDirect

Acta Materialia 94 (2015) 271–280

Acta MATERIALIA

www.elsevier.com/locate/actamat

On the determination of stress profiles in expanded austenite by grazing incidence X-ray diffraction and successive layer removal

Frederico A.P. Fernandes,[1] Thomas L. Christiansen, Grethe Winther and Marcel A.J. Somers*

Technical University of Denmark, Department of Mechanical Engineering, Produktionstorvet 425, DK-2800 Kgs. Lyngby, Denmark

Received 2 February 2015; revised 22 April 2015; accepted 26 April 2015
Available online 21 May 2015

Abstract—Surface layers of expanded austenite resulting from nitriding typically exhibit large gradients in residual stress and composition. Evaluation of residual-stress profiles is explored by means of grazing incidence X-ray diffraction (GI-XRD), probing shallow depths, combined with successive layer removal. Several factors complicating the stress determination are analysed and discussed: (1) ghost stresses arising from a small variation in the shallow information depths probed with GI-XRD, (2) selection of the grain interaction model used to calculate the X-ray elastic constants for conversion of lattice strains into residual stress and (3) the composition dependence of these elastic constants.

Keywords: Low temperature surface hardening; Gas nitriding; Expanded austenite; X-ray diffraction; Stress analysis

1. Introduction

Although the first exploitation of expanded austenite dates back about 30 years [1,2], it continues to be a topic of research and discussion in the current literature. While plasma-based processes for the surface hardening of stainless steel have dominated the first 15 years of intensive investigation, later years have seen the advent of and a growing interest in gaseous processing [3,4]. The transformation of the surface region of austenitic stainless steel into a case of expanded austenite is associated with a spectacular improvement of the wear and fatigue performance, while the corrosion performance remains unaffected, or is even improved [5].

Expanded austenite is obtained by interstitially dissolving colossal amounts of nitrogen and/or carbon into austenite [6,7] at a temperature that is too low to allow long range diffusion of substitutionally dissolved components in the alloy. Accordingly, the depth of the hard case brought about is entirely the result of (stress-assisted) interstitial diffusion of carbon/nitrogen atoms in austenite. No new phase develops and expanded austenite should be considered as a diffusion zone in austenite. As a consequence of the high content of interstitially dissolved nitrogen/carbon in existing austenite grains huge compressive residual stress is built up along with the interstitial concentration profile. Compressive residual stress values of 7.5 GPa in the plane parallel to the surface have been reported for probing the 200 reflection of expanded austenite [3]. Moreover, plastic accommodation and associated relaxation of the enormous composition induced stresses were observed as grain push-out [7,8], lattice rotations [9–11] and enhanced stacking fault densities [12].

Depth-resolved quantification of composition-induced stress profiles in expanded austenite with X-ray diffraction techniques is far from trivial, as apart from an influence of the stress gradient on the local lattice spacing, also gradients in composition and stacking-fault density affect the lattice spacing [6]. Both destructive and non-destructive measurement strategies and data correction procedures have been published in the latter years to unravel the contributions of stress, composition and stacking fault gradients on lattice spacing profiles [13,14]. The application of an asymmetric path by grazing incidence allows X-rays to probe only a very shallow depth range under the exposed surface and thus minimises the effect of gradients. In the present article this technique is combined with successive layer removal to analyse the effects of steep gradients in stress and composition on the determined stress profiles in an expanded austenite case obtained by gaseous nitriding.

1.1. X-ray diffraction stress analysis in expanded austenite zones

Surface layers obtained by thermochemical surface engineering can usually be assumed to experience a rotationally symmetric biaxial state of macroscopic (Type 1)

* Corresponding author at: Technical University of Denmark, Department of Mechanical Engineering, Produktionstorvet 425, DK-2800 Kgs. Lyngby, Denmark.

[1] Present Address: São Paulo State University (UNESP), Ilha Solteira, SP, Brazil.

http://dx.doi.org/10.1016/j.actamat.2015.04.040
1359-6462/

stress, implying that $\sigma_{11} = \sigma_{22} = \sigma_{\parallel}$, which leads to a simplification of the dependence of the lattice strain, ε_{ψ}^{hkl}, of the family of lattice planes $\{hkl\}$ on the tilt angle ψ:

$$\varepsilon_{\psi}^{hkl} = \frac{d_{\psi}^{hkl} - d_{\varepsilon=0}^{hkl}}{d_{\varepsilon=0}^{hkl}} = 1/2S_2^{hkl}\sigma_{\parallel}\sin^2\psi + 2S_1^{hkl}\sigma_{\parallel} \quad (1)$$

where d_{ψ}^{hkl} is the lattice spacing for the same $\{hkl\}$ planes in the direction defined by ψ, $d_{\varepsilon=0}^{hkl}$ is the strain-free lattice spacing and S_1^{hkl} and $1/2S_2^{hkl}$ are X-ray elastic constants (XECs) depending on the material and on the $\{hkl\}$ indices. The strain-free lattice spacing, $d_{\varepsilon=0}^{hkl}$, in Eq. (1) is probed for the so-called strain-free measurement direction, $\psi_{\varepsilon=0}$, which is obtained from equating Eq. (1) to zero and rearranging terms:

$$\sin^2\psi_{\varepsilon=0} = \frac{-2S_1^{hkl}}{1/2S_2^{hkl}}. \quad (2)$$

After determination of $d_{\varepsilon=0}^{hkl}$ it is straightforward to obtain the stress from Eq. (1).

The standard method known as the "$\sin^2\psi$" method employs the symmetric Bragg–Brentano geometry and leads to a significant variation of the information depth for different tilt angles. For the case of lattice spacing gradients these variations in information depth with tilt angle lead to ghost or fictitious stresses [15]. Avoiding such artefacts requires an effective correction procedure of the obtained lattice spacing results [13–15]. Successful application of the correction method firstly proposed in Ref. [15] for unravelling stress- and composition–depth profiles in γ'-Fe_4N_{1-x} surface layers, was demonstrated for carbon- [16] and nitrogen-expanded austenite [3]. In these attempts a symmetrical diffraction method was applied, associated with relatively large (variations in) information depth, leading to broad asymmetric X-ray line profiles as a consequence of the very broad composition range for, in particular, nitrogen-expanded austenite. If a grazing incidence angle is applied, only a shallow depth is probed and the error made in the evaluated lattice spacing is much smaller, because narrower X-ray line profiles are obtained, while the variation of the information depth with ψ tilting is reduced importantly. In principle, an appropriate choice of the combination of grazing incidence angle with tilt angle allows probing the material at the same information depth for a range of tilt angles [17]. In this way several information depths can be probed non-destructively, as was demonstrated experimentally for vapour deposited Ni-layers [18] and ground Al_2O_3 [19]. In both these applications the samples investigated had only a stress–depth profile and were uniform in composition within the investigated depth range. Provided that the surface layer (or case) investigated diffracts independently from the bulk (or core) the maximum information depth that can be probed by this non-destructive technique corresponds to half the thickness of the surface layer, which for expanded austenite is associated with broad X-ray line profiles as a consequence of the composition–depth profile. Therefore, in this investigation, successive layer removal was applied combined with grazing incidence X-ray diffraction. Instead of keeping the information depth constant by varying the grazing incidence angle with ψ, in the present work the grazing incidence was kept fixed for all applied ψ tilts. Applying grazing incidence the lattice planes are actually probed in a direction that is tilted with respect to the surface normal even when no actual rotation, χ, over the Ψ-axis perpendicular to the Ω ($\omega/2\theta$)-axis is applied in the goniometer [16]. The effective tilt angle ψ that should be accounted for in the calculation of the stress is therefore:

$$\cos\psi = \cos\chi \cdot \cos(\theta - \alpha) \quad (3)$$

where α is the fixed grazing incidence angle, χ is the rotation angle around the Ψ-axis and 2θ is the Bragg angle.

The applicability of this method for the present case will be further explored in Section 4.1.

Table 1. X-ray elastic constants for the {111} and {200} family planes according to different models. The values are given in 10^{-6} MPa^{-1}. The single crystal elastic constants from which the Voigt and Reuss constants are calculated for a randomly textured polycrystal are $s_{11} = 10.7$ MPa^{-1}, $s_{44} = 8.60$ MPa^{-1}and $s_{12} = -4.25$ MPa^{-1} [30]. The Kröner–Eshelby constants are from [31].

	Kröner–Eshelby		Voigt		Reuss	
	111	200	111	200	111	200
S_1^{hkl}	−1.1	−2.3	−1.3	−1.3	−0.7	−4.3
$1/2S_2^{hkl}$	5.1	8.83	6.01	6.01	4.3	15.0

1.2. X-ray elastic constants and grain interaction models

The XECs can be calculated from the single crystal elastic constants, adopting an appropriate model for the elastic interaction between the grains in a polycrystal. The two extreme interaction models are the Voigt [20] assumption that all grains experience the same strain and the Reuss [21] model based on all grains having equal stress. Other interaction models have been devised, including self-consistent approaches by Eshelby [22] and Kröner [23], where the (anisotropic) grains probed interact with a matrix with isotropic properties averaging over all grain orientations. The Voigt and Reuss approaches were proven by Hill [24] to be the upper and lower bounds for the elastic modulus of a bulk polycrystal. This has suggested averaging of the results of the two models [25]. For the special conditions at free surfaces and two-dimensional grain interaction in the plane of the surface, the Vook–Witt model [26,27] assumes equal strains in the surface plane and a zero stress perpendicular to the surface, whilst the inverse Vook–Witt model [28] assumes equal stresses in the surface plane and equal strains perpendicular to the surface.

Irrespective of the grain interaction model (GIM) adopted, the single crystal elastic constants of the material considered are essential components in the calculation of the XECs for the polycrystal. Single crystal constants have not yet been determined for expanded austenite and the values reported for alloys with Cr and Ni contents in the range 12–18%, e.g. [29], have therefore often been used [30]. XECs derived from such single crystal values are listed in Table 1. XECs from the Kröner–Eshelby model (as given in [31]) are employed to discuss the effects of gradients in composition and stress, while the upper and lower bounds by Voigt and Reuss are the basis for discussion of GIM selection. Finally, the effects of nitrogen content on the XECs are analysed.

2. Experimental

2.1. Sample preparation

Discs with a diameter of 20 mm and a thickness of 3 mm were cut from a solution treated bar of AISI 316L with the

following chemical composition: Fe–0.019C–0.067N–1.47 Mn–0.40Si–16.26Cr–10.05Ni–2.02Mo–0.47Cu (wt.%). The flat surfaces of the specimens were ground and polished at a final step of 3 μm diamond paste to achieve a mirror-like surface finish.

Gaseous thermochemical treatments were conducted in a hermetic LAC PKRC55 furnace at 430 °C for 20 h applying 2 L/min of pure ammonia (NH_3). Prior to nitriding, activation of the samples to remove the protective oxide layer was carried out *in situ* with a proprietary treatment.

For metallographic investigation cross sections of the nitrided samples were hot mounted, followed by grinding and polishing for reflected light microscopy investigations in a Zeiss Neophot 32. To reveal the microstructural features Kalling's reagent 1 was employed for approximately 15 s. The embedded cross sections were also used for measuring the Vickers micro-hardness profile with a Future Tech model FM-700 hardness tester, applying a load of 5 gf and a dwell time of 5 s.

2.2. Glow discharge optical emission spectroscopy (GD-OES)

The composition of the nitrided case was determined with Glow Discharge Optical Emission Spectroscopy (GD-OES), using a Horiba Jobin Yvon GD profiler 2. The plasma applied for controlled sputtering of the sample surface was 1000 Pa pressure and 40 W. Concentration profiles of substitutionally and interstitially dissolved components were obtained using a selection of stainless steel reference materials and γ'-Fe_4N on pure iron as a nitrogen reference.

2.3. X-ray diffraction phase analysis and lattice spacing-depth profiling

X-ray diffraction experiments were performed using a Bruker AXS D8 diffractometer equipped with a Cr-tube source with a characteristic wavelength of 2.28976 Å. The equipment was operated employing a voltage and current of 40 kV and 40 mA. X-ray diffraction was applied for both phase identification and lattice spacing profiling for residual stress analysis.

For phase analysis, diffractograms were determined using a linear focus and Bragg–Brentano symmetrical geometry. The measurements cover the range 40–100° 2θ, including the 111 and 200 reflections of (expanded) austenite, applying a step-size of 0.03° 2θ and measurement time per step of 5 s.

To obtain lattice spacing-depth profiles over the thickness of the nitrided case the diffractometer was configured in point focus mode using a vanadium window to remove Cr K_β radiation. The 111 and 200 reflections of austenite and expanded austenite were included in all scans ranging from 53 to 85° 2θ, applying a step-size of 0.05° 2θ for 5 values of χ (0, 25°, 38°, 49°, 60°) at a measurement time of 6 s. It is common practice to use high 2θ angle reflections for stress analysis. However, since the 220 and 311 reflections were very broad and had poor intensity, only the 111 and 200 reflections could be used for X-ray stress determination. From the investigation of stress-free stainless steel powder the instrumental influence of applying reflections in this low 2θ range was determined to be less than 100 MPa. This contribution is considered negligible.

Successive removal of approximately 1-μm-thick sublayers of expanded austenite was realised by gently polishing the treated surface with a 3 μm diamond suspension and monitoring the weight loss of the sample using an analytical balance. After each step the X-ray experiments were repeated.

3. Results

3.1. Metallography

A reflected light micrograph of the sample gaseously nitrided at 430 °C for 20 h in pure ammonia is shown in Fig. 1. The nitrided zone exhibits the typical morphology of expanded austenite (γ_N) produced on low temperature nitriding austenitic stainless steel [7]. Layer thickness measurements on the cross section yielded an average zone thickness of 13 ± 1 μm.

The Vickers hardness profile is given in Fig. 2. A hardness of about 11.8 GPa is reached near the surface and is maintained throughout the nitrided case. Approaching the layer/substrate interface, the hardness decreases abruptly with depth reaching 2.15 GPa at around 13 μm, which corresponds to the zone thickness. The low substrate hardness is consistent with the supplied material condition.

3.2. Composition analysis

Fig. 3 presents the nitrogen-depth profile in atomic percentage (at.%) and a series of X-ray diffractograms obtained by applying the Bragg–Brentano symmetric geometry. The profile obtained by GD-OES, shown in Fig. 3(a), confirms the presence of a nitrogen-rich zone. Nitrogen reaches values as high as 35 at.% at the surface and its concentration decreases steeply within 15 μm. The arrows on the GD-OES profile indicate the approximate positions where the XRD diffractograms were taken below the surface (Fig. 3(b)).

The X-ray diffractograms in Fig. 3(b) show the 111 and 200 reflections for both austenite and expanded austenite in the scattering angle range 50 to 85° 2θ. At the surface of the nitrided sample where the nitrogen concentration is highest,

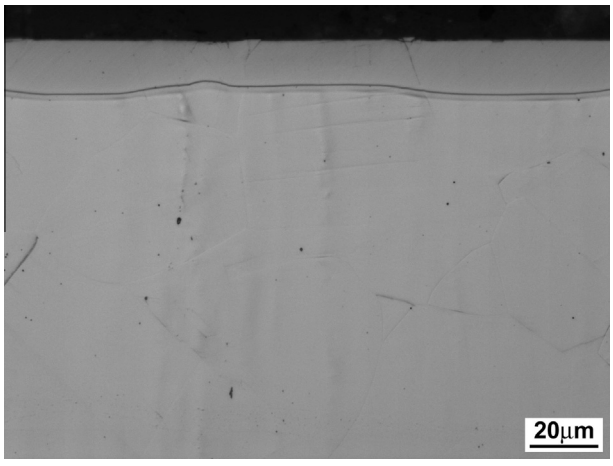

Fig. 1. Reflected light micrograph from the cross section of the AISI 316L steel nitrided at 430 °C for 20 h in pure NH_3.

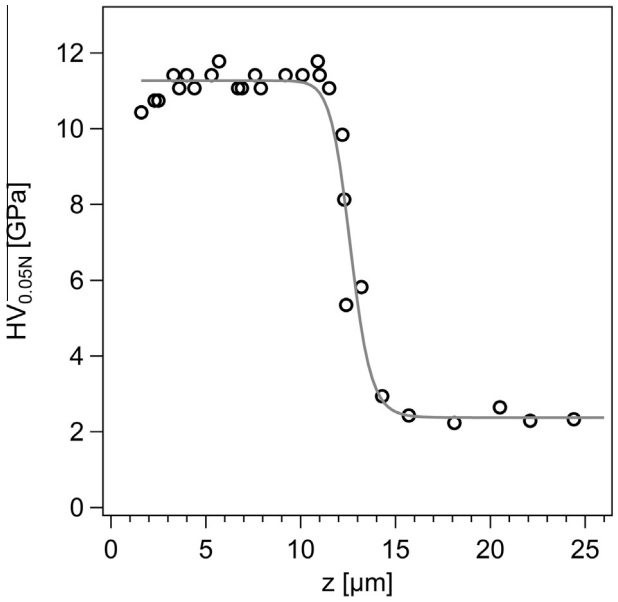

Fig. 2. Vickers hardness ($HV_{0.05N}$) profile of the AISI 316L steel nitrided at 430 °C for 20 h in pure ammonia.

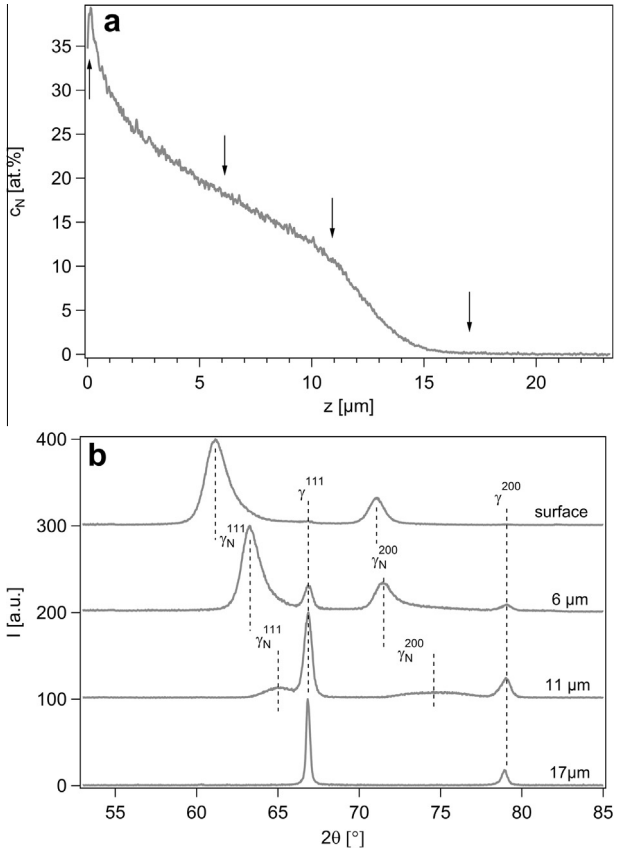

Fig. 3. (a) Nitrogen profile obtained with GD-OES and (b) X-ray diffractograms of the AISI 316L steel gas nitrided at 430 °C for 20 h obtained by symmetric X-ray diffraction. From top to bottom: as-nitrided and after removing 6 μm, 11 μm and 17 μm; the latter corresponds to un-treated bulk austenite. The arrows in the GD-OES profile show the (approximate) positions of the surface positions for the diffractograms in b.

the reflections are very broad and a large peak-shift to lower Bragg angle is noticed as compared to untreated austenite. After removing 6 μm by polishing, the expanded austenite peaks shift to higher Bragg angles and additionally the 111 and 200 reflections from the substrate also appear due to the penetration of the X-rays, indicating that a diffracted intensity-weighted average over the nitrided zone is obtained. At a depth of 6 μm the nitrogen concentration is about 20 at.% according to the GD-OES profile. After removing 11 μm the nitrogen concentration drops to 10 at.% and the substrate peaks become prominent. In this case only a few microns of expanded austenite remain. Interestingly, the 200 reflection of γ_N is very broad. At a depth of approximately 17 μm below the original surface the nitrided zone is removed entirely and only the substrate reflections of austenite remain. Note that the width of these reflections is considerably narrower than for expanded austenite.

3.3. X-ray diffraction lattice spacing analysis

For the actual experiments, the as-measured lattice spacing values, $\left\langle d_{\psi}^{hkl} \right\rangle$, were obtained from the centroid position of the 111 and 200 reflections. Near the case/core transition the contribution from the substrate was also included in determining the centroid peak position, because expanded austenite and substrate are inseparable close to the substrate. All $\sin^2\psi$ plots determined for the 111 and 200 reflections after performing several consecutive removal steps were published in a previous publication [32]. Fitting straight lines through the $\left\langle d_{\psi}^{hkl} \right\rangle$ vs. $\sin^2\psi$ dependencies, the slopes, $\Delta\left\langle d_{\psi}^{hkl} \right\rangle / \Delta \sin^2\psi$, and intercepts, $\left\langle d_{\psi=0}^{hkl} \right\rangle$, of the $\sin^2\psi$ plots were obtained, as well as the uncertainties (see Fig. 4). Both the slopes and the intercepts vary relatively smoothly throughout the layer. Down to a depth of about 11 μm, the slopes are negative, indicating compressive stresses. In the depth range 11–13 μm the slopes are slightly positive, which would indicate tensile stresses. Finally the slopes level off to a slightly negative value further into the substrate. The intercepts decrease continuously and attain a plateau value for depths above 13 μm. This depth range agrees favourably with the hardness and composition profiles in Figs. 2 and 3(a), where a large change is observed at a depth range 11–13 μm. Hereafter constant intercept values are obtained. It is mentioned that not all $\left\langle d_{\psi}^{hkl} \right\rangle$ vs. $\sin^2\psi$ dependencies were strictly linear. In particular, the $\sin^2\psi$ plots in the transition region from the expanded austenite case to the unaffected core showed non-linearity, as reflected by the relatively large error bars for, in particular, the slope (Fig. 4). As follows from the error the bars indicated in Fig. 4, generally the evaluation of the 111 reflection for stress analysis provides a more reliable result than the 200 reflection.

4. Discussion

4.1. Ghost stress effects in GI-XRD investigation of expanded austenite

Below, an evaluation of the applicability of the applied method with constant grazing incidence angle is given by

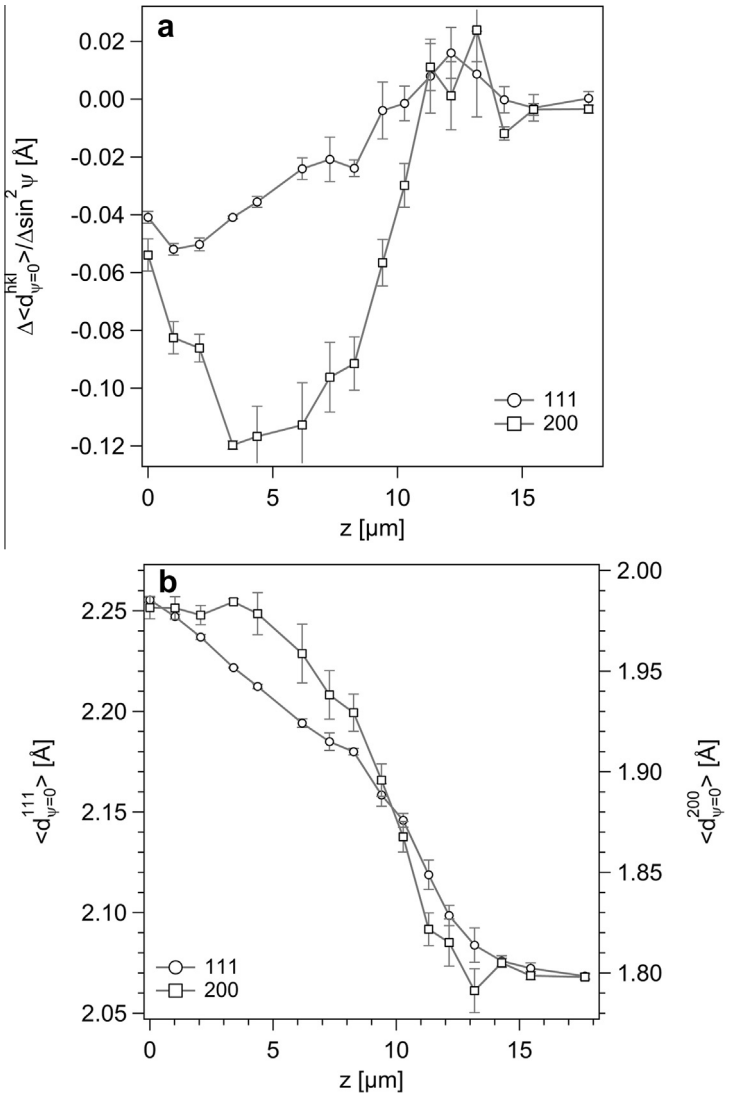

Fig. 4. Slopes, $\Delta\left\langle d_{\psi}^{hkl}\right\rangle/\Delta\sin^2\psi$, and intercepts, $\left\langle d_{\psi=0}^{hkl}\right\rangle$, of the $\sin^2\psi$ plots presented in Ref. [32]. Error bars reflect the variation in slope and intercept as obtained from regression analysis.

a simulation of the current X-ray experiment and assessment of the ghost stresses that arise from the combination of a variation in the information depth with χ rotation. The information depth, τ_{ψ}^{hkl}, for a certain family of lattice planes probed, is taken as the depth weighted over the diffracted intensity, and is given by [33]:

$$\tau_{\psi}^{hkl} = \left\langle z_{\psi}^{hkl}\right\rangle = \frac{\int_0^{\infty} z\cdot e^{-\mu k_{\psi}^{hkl} z}\times dz}{\int_0^{\infty} e^{-\mu k_{\psi}^{hkl} z}\times dz} = \frac{1}{\mu k_{\psi}^{hkl}} \tag{4}$$

with μ the linear absorption coefficient of the applied X-radiation in the phase probed and

$$k_{\psi}^{hkl} = \frac{1}{\cos\chi}\times\left(\frac{1}{\sin\alpha}+\frac{1}{\sin(\theta-\alpha)}\right) = \frac{\cos(\theta-\alpha)}{\cos\psi}\times\left(\frac{1}{\sin\alpha}+\frac{1}{\sin(\theta-\alpha)}\right) \tag{5}$$

The variation of the information depth probed with Cr K_{α} radiation (wavelength $\lambda = 2.28976$ Å) is given for the approximate 2θ positions of the 111 and 200 line profiles of expanded austenite in Fig. 5 for a grazing incidence angle of 2°. Clearly, the variation of the information depth with $sin^2\psi$ is the same within the Bragg angle range that contains the 111 and 200 reflections: 53–82° 2θ. Hence, experiments on 111 and 200 line profiles as investigated in the experimental part of the present work essentially contain the same diffracted intensity weighted information.

Ghost stress effects for the chosen measurement geometry were estimated for the following conditions:

- A stress-free expanded austenite case on a stress-free austenite core with a realistic composition–depth profile. This is a purely hypothetical condition, which is used to demonstrate how a composition gradient affects the measurements.
- A realistic stress distribution in expanded austenite cases, i.e. a plateau value of several GPa's in the expanded austenite zone gradually decreasing to zero stress in the substrate, without a composition profile. Also this is a hypothetical case for expanded austenite, but it is used to demonstrate the principal applicability of the stress measurement strategy.

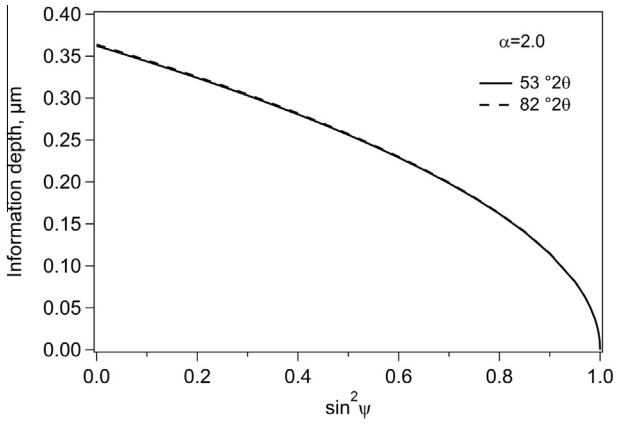

Fig. 5. Variation of information depth, τ_{ψ}^{hkl}, in expanded austenite with $sin^2\psi$. The information depth is independent of the Bragg angle 2θ within the range wherein the 111 and 200 reflections lie, i.e. 53–82° 2θ.

Details of the calculations for these conditions are as follows.

4.1.1. Ghost stress in stress-free expanded austenite with a composition profile

The experimental composition profile in expanded austenite as determined with GD-OES and given in Fig. 3(a) was taken as the composition distribution. Assuming a linear relation between the lattice parameter of expanded austenite and the nitrogen content and adopting the lattice spacing values at $y_N = 0$ and $y_N = 0.6$ [7] for this linearisation, the composition profile was converted into lattice-spacing profiles for the {111} and {200} lattice planes and described by polynomials [34]:

$$d_{\psi}^{hkl} = \sum_{j=0}^{n} A_{\psi,j}^{hkl} (z)^j \tag{6}$$

In an X-ray diffraction experiment the lattice spacing obtained, $\left\langle d_{\psi}^{hkl} \right\rangle$, is the lattice spacing profile weighted over the diffracted intensity:

$$\left\langle d_{\psi}^{hkl} \right\rangle = \frac{\int_0^{\infty} \left\{ \sum_{j=0}^{n} A_{\psi,j}^{hkl} (z)^j \right\} \times e^{-\mu k_{\psi}^{hkl} z} \times dz}{\int_0^{\infty} e^{-\mu k_{\psi}^{hkl} z} \times dz} \tag{7}$$

It can be demonstrated that $\left\langle d_{\psi}^{hkl} \right\rangle$ is the Laplace transformation of $d_{\psi}^{hkl}(z)$ in τ space [34]:

$$\left\langle d_{\psi}^{hkl} \right\rangle = \sum_{j=0}^{n} A_{\psi,j}^{hkl} \left(\tau_{\psi}^{hkl} \right)^j \times j! \tag{8}$$

For calculation of the diffracted intensity-weighted lattice spacing as a function of information depth, the following procedure was pursued. Lattice spacing profiles $d_{\psi}^{hkl}(z)$ were calculated for 5 values of ψ, corresponding to the χ values applied in the experimental part of this work, i.e. $\chi = 0$, 25°, 38°, 49°, 60° (cf. Eq. (3) and Section 2.3) and fitted with polynomials according to Eq. (6). Since no stress is assumed, $d_{\psi}^{hkl}(z)$ is independent of ψ. The order, n, of the polynomials in Eq. (6) was chosen such that a smooth fit was obtained through the data in the entire expanded austenite zone; this was achieved for $n = 9$. From the coefficients of the fitted polynomia and the associated information depths the diffraction-intensity weighted lattice parameter is straightforwardly obtained from Eq. (8).

Subsequently, a sublayer thickness equal to the experimentally removed thicknesses was removed from the d_{ψ}^{hkl} profiles, thereby creating a new surface, and the remaining composition data were fitted again with Eq. (6), giving new values for $A_{\psi,j}^{hkl}$, τ_{ψ}^{hkl} and $\left\langle d_{\psi}^{hkl} \right\rangle$. This procedure was repeated until the unaffected core was reached. The order of the polynomials varied from $n = 9$ close to the original surface to $n = 3$ close to the unaffected core.

For each sublayer removal a $\left\langle d_{\psi}^{hkl} \right\rangle$ vs. $sin^2\psi$ plot was calculated. Using the XEC calculated with the Kröner–Eshelby model (cf. Table 1), both the (ghost) stress and the strain-free lattice spacing were evaluated using Eqs. (1) and (2). The thus calculated stress and strain-free lattice spacing values were assigned to information depth that applies for the strain-free direction, $\tau_{\psi_{\varepsilon=0}}^{hkl}$. In Fig. 6 the lattice parameter in the strain free direction, $\left\langle d_{\psi_{\varepsilon=0}}^{200} \right\rangle$, is given vs. the information depth, $\tau_{\psi_{\varepsilon=0}}^{200}$, and compared to the actual lattice spacing profiles, $d_{\psi_{\varepsilon=0}}^{200}(z)$, used as input for the simulated X-ray diffraction experiments. A very good correspondence is obtained between the "as measured" profile and the input data, illustrating that the grazing incidence method is indeed associated with a very shallow

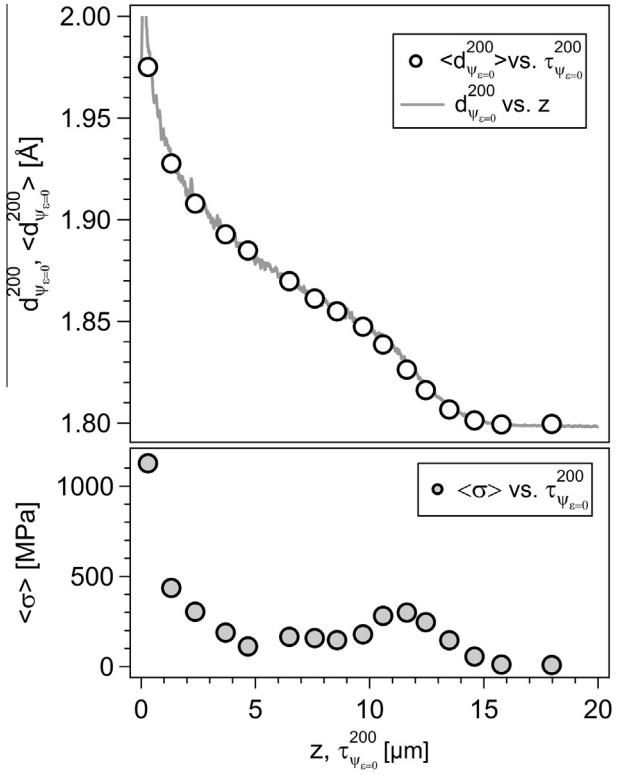

Fig. 6. Comparison of the lattice spacing vs. real depth profile as calculated from the GDOES profile for 200 (drawn line) and the $\left\langle d_{\varepsilon=0}^{200} \right\rangle$ values calculated with Eq. (7) presented vs. the information depth, $\tau_{\psi_{\varepsilon=0}}^{200}$, as calculated with Eq. (4) (open circles). The lower part of the graph shows the stress, $\langle\sigma\rangle$, evaluated from $\left\langle d_{\psi}^{200} \right\rangle$ *s.* $\sin^2\psi$ relations; these stresses are fictitious, i.e. ghost stresses, and arise from the variation of $\tau_{\psi_{\varepsilon=0}}^{200}$ with ψ.

information depth and an accurate determination of a lattice spacing profile.

In the lower part of Fig. 6 the stress value $\langle\sigma\rangle$ evaluated from the slope of the $\left\langle d_{\psi}^{200}\right\rangle$ vs. $sin^2\psi$ plots is given vs. $\tau_{\psi_{\varepsilon=0}}^{200}$. Clearly, substantial tensile ghost stress values were obtained, particularly in the steep parts of the nitrogen concentration profile. As no stress was present *a priori*, these calculated tensile stresses are exclusively an artefact of the chosen evaluation procedure, and are thus ghost stresses. Although shallow depth ranges of the lattice profile were "probed" in the simulations, still ghost stresses can exceed 1 GPa in the region close to the surface where a very steep gradient of the lattice parameter applies. This ghost stress is entirely attributed to the variation of the information depth, from about 0.35 μm to about 0.18 μm (cf. Fig. 5), with χ angle.

4.1.2. Ghost stress in expanded austenite with a stress profile

Calculations of the ghost stress in an expanded austenite zone with only a stress profile were performed for a stress–depth profile, $\sigma(z)$, with a constant value σ_+ that gradually declines to a stress level σ_- in the substrate (see Fig. 7):

$$\sigma(z) = \sigma_- + \frac{(\sigma_+ - \sigma_-)}{1 + \left(\frac{z_{1/2}}{z}\right)^r} \tag{9}$$

with $\sigma_+ = -3.5$ GPa, $\sigma_- = 0$, $z_{1/2} = 11.2$ μm and $r = -11$.

From Eq. (1), taking as the lattice parameter $a = d_{\varepsilon=0}^{hkl} \cdot \sqrt{h^2 + k^2 + l^2} = 3.60$ Å, profiles $d_{\psi}^{hkl}(z)$ were calculated for 5 values of ψ, corresponding to the χ values applied in the experimental part of this work, i.e. $\chi = 0$, 25°, 38°, 49°, 60° and fitted with polynomials according to Eq. (6). In contrast with the results in Section 4.1.1, for this case the 5 lattice spacing profiles are *not* identical. The calculation of diffracted intensity-weighted lattice spacing profiles is fully analogous to the description given in Section 4.1.1, albeit that five ψ values have to be considered after each sublayer removal. Evaluating the stress $\langle\sigma\rangle$ from the slope of the $\left\langle d_{\psi}^{200}\right\rangle$ vs. $sin^2\psi$ plots, the results given in Fig. 7 were obtained. The "as measured" stress–depth profile is in excellent correspondence with the adopted stress–depth profile and the ghost stresses $\langle\sigma\rangle - \sigma$ in the lower part of the graph are negligible (<2% of the absolute stress value) and within experimental accuracy of the method. The absence of a trend in the ghost stresses suggests that they result from the accuracy of the polynomial to fit the lattice spacing depth profiles.

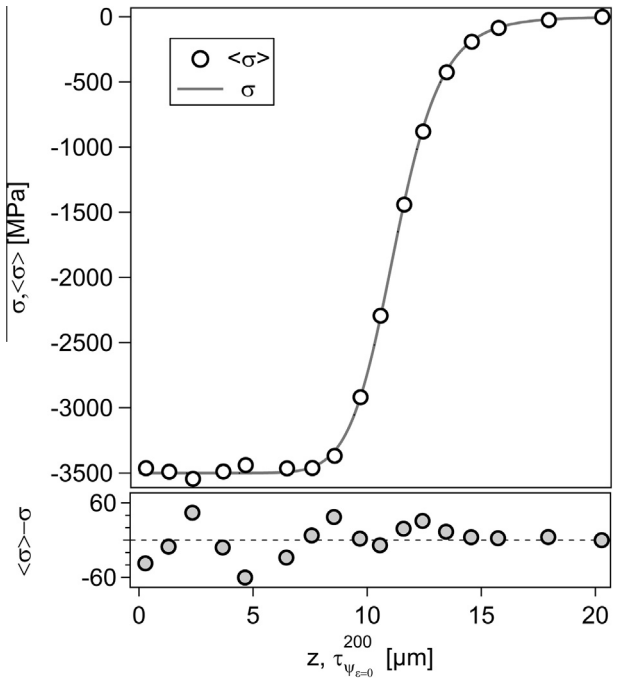

Fig. 7. Comparison of the stress–depth profile (Eq. (9)) assumed to be present over the thickness of the nitrided case (drawn line) and the stress values determined from $\left\langle d_{\psi}^{200}\right\rangle$ vs. $sin^2\psi$ plots and assigned to the information depth, $\tau_{\psi_{\varepsilon=0}}^{200}$ (open circles). The lower part of the graph shows the ghost stress, $\langle\sigma\rangle - \sigma$ vs. $\tau_{\psi_{\varepsilon=0}}^{200}$.

4.2. Evaluation of grain interaction models for stress determination

Application of Eq. (2) using the XEC's from Table 1 and the relations $\langle a^{111}\rangle = \left\langle d_{\psi=0}^{111}\right\rangle \times \sqrt{3}$ and $\langle a^{200}\rangle = \left\langle d_{\psi=0}^{200}\right\rangle \times 2$ to find values for the strain-free lattice parameter from the experimental data in Fig. 4 gives the profiles in Fig. 8(a) for Reuss and Voigt Grain Interaction Models (GIMs). The thus obtained strain-free lattice parameter profiles are generally in good overall agreement with each other and the lattice parameter profile given in Fig. 8(a) as calculated from the GD-OES profile in Fig. 3(a) (see Section 4.1.1 for this calculation). The strain-free lattice parameters obtained from the positions of 111 and 200 reflections appear to be closer to each other for the Reuss GIM than for the Voigt GIM.

The corresponding obtained stress profiles with the Voigt and Reuss models for the two reflections studied are depicted in Fig. 8(b). If the models are correct, the stress should be independent of the probed family of lattice planes. As for the strain-free lattice parameter profiles, a major discrepancy between 111 and 200 is observed if the stress values are obtained with the Voigt GIM, while a fair correspondence is obtained if the Reuss GIM is applied.

At the transition from case to core tensile stresses are seen in Fig. 8(b). However, at this depth the analysis is affected by: (1) the effect of using the centroid position of the *hkl* line profile for evaluating $\left\langle d_{\psi}^{hkl}\right\rangle$, (2) non-linearity of the $\left\langle d_{\psi}^{hkl}\right\rangle$ vs. $\sin^2\psi$ dependencies resulting in positive slopes and (3) the relative importance of ghost stress effects in the transition region (see Section 4.1.1). Hence, it cannot be concluded whether an actual tensile stress component occurs at the case-core transition or whether this is an artefact of the applied measurement and data evaluation procedures.

For the present morphology the grains at the free surface have a grain size exceeding 30 μm, which is larger than the layer depth (13 μm) and considerably larger than the information depth used in this work. Consequently, the expanded austenite zone has developed into grains that are bound by the sample surface and by neighbouring crystals only in two dimensions. Hence, the crystallites have the freedom to expand elastically in the direction of the surface normal. One may therefore argue that the (inverse) Vook–Witt GIM developed for columnar grain structures, as in columnar thin films, would apply. Irrespective of surface effects, the upper and lower bounds of the elasticity

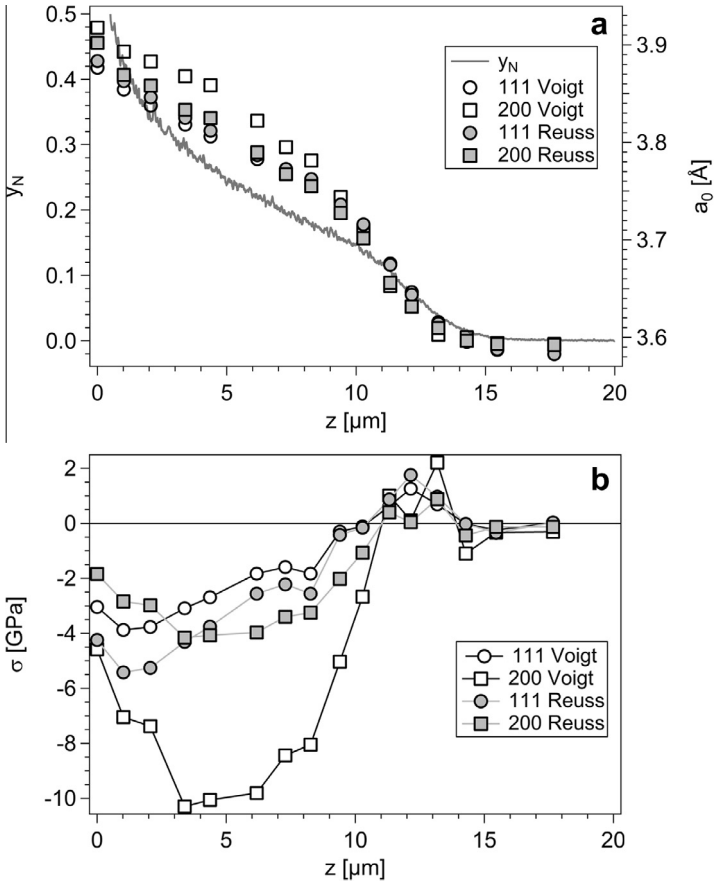

Fig. 8. (a) Strain-free lattice parameter a_0 and (b) residual stress ($\sigma_\parallel$) vs. the removed sublayer thickness, z, for the 111 and 200 reflections of expanded austenite with XECs calculated with Reuss and Voigt GIM (see Table 1). For comparison the composition profile as determined with GD-OES is included (cf. Fig. 3). Scaling of left and right ordinates was done using lattice parameter composition dependencies in Ref. [7] (see Section 1.2).

modulus as well as the stress are defined by the Voigt and Reuss models, respectively. The Voigt model should therefore predict a larger absolute stress level than predicted by Reuss. This is the case for the 200 reflection but not for 111, suggesting additional problems not associated with selection of the appropriate GIM. In this respect, it should be realised that the effect of dissolving nitrogen in austenite on the XECs has not been accounted for and is not quantitatively known.

4.3. Effect of nitrogen content on elastic constants of austenite

The effect of the nitrogen content on the XECs is analysed based on Eq. (1) and the experimentally determined slopes and intercepts of the $\left\langle d_\psi^{hkl} \right\rangle$ vs. $\sin^2\psi$ plots for each layer (Fig. 4). The biaxial residual stress, $\sigma_\parallel$, is per definition the same for the 111 and 200 reflections. The slope, B^{hkl}, of a $\left\langle d_\psi^{hkl} \right\rangle$ vs. $\sin^2\psi$ plot equals $\frac{1}{2}S_2^{hkl} \times \sigma_\parallel \cdot d_{\varepsilon=0}^{hkl}$, while the intercept, G^{hkl}, equals $\left(2S_1^{hkl} \cdot \sigma_\parallel + 1\right) \times d_{\varepsilon=0}^{hkl}$. For each reflection, this gives two equations with $2S_1^{hkl}$, $\frac{1}{2}S_2^{hkl}$, $d_{\varepsilon=0}^{hkl}$ and $\sigma_\parallel$ as unknowns.

By expressing the XECs $2S_1^{111}$, $\frac{1}{2}S_2^{111}$ and $2S_1^{200}$ relative to $\frac{1}{2}S_2^{200}$, the unknown $\sigma_\parallel$ is eliminated and the following set of, altogether 3, equations is obtained:

$$\frac{2 \times S_1^{hkl}}{\frac{1}{2}S_2^{200}} = \frac{G^{hkl} - d_{\varepsilon=0}^{hkl}}{B^{200}} \times \frac{d_{\varepsilon=0}^{200}}{d_{\varepsilon=0}^{hkl}} \tag{10a}$$

$$\frac{\frac{1}{2}S_2^{111}}{\frac{1}{2}S_2^{200}} = \frac{B^{111}}{B^{200}} \times \frac{d_{\varepsilon=0}^{200}}{d_{\varepsilon=0}^{111}} \tag{10b}$$

In the absence of stacking faults, the strain-free lattice spacings $d_{\varepsilon=0}^{hkl}$ may be expressed in terms of the strain-free lattice parameter, i.e. $d_{\varepsilon=0}^{hkl} = a_0/\sqrt{h^2+k^2+l^2}$. Previously, it has been shown that homogeneous, stress-free nitrogen-expanded austenite with a high nitrogen content has a faulted fcc lattice and that, as a consequence, on comparing lattice spacings for different *hkl*, the role of stacking faults should be taken into consideration [4,12,14]. Here, the effect of stacking faults is estimated based on the equation by Warren [35],[1] relating the peak shift $\Delta(2\theta)_\beta^{hkl}$ to the stacking fault probability β:

$$\Delta(2\theta)_\beta^{hkl} = 0.2756 \times \beta \cdot H_{hkl} \times \tan(\theta_0^{hkl}) \tag{11}$$

[1] It is noted that a prediction of the effect of stacking faults on *hkl* dependent peak shifts by the Warren approach is inaccurate, but that a reasonable prediction is obtained for the 200 and 111 reflections and relatively small stacking fault densities, as investigated here.

where $H_{111} = \frac{1}{4}$, $H_{200} = -\frac{1}{2}$ and $\theta_0^{hkl} = \arcsin\left(\frac{\lambda}{2a_0/\sqrt{h^2+k^2+l^2}}\right)$.

The resulting $d_{\varepsilon=0}^{hkl}(a_0, \beta)$ is given by:

$$d_{\varepsilon=0}^{hkl}(a_0, \beta) = \frac{\lambda}{2\sin\left(\theta_0^{hkl} + \frac{1}{2}\Delta(2\theta)_\beta^{hkl}\right)}. \quad (12)$$

As an initial guess, the strain-free lattice parameter $a_{\varepsilon=0}$ is estimated to lie within the interval [3.59Å;4.10Å] and the stacking fault probability β is assumed to lie within the interval [0;0.03]. By varying $a_{\varepsilon=0}$ and β in steps of 0.01 Å and 0.01, respectively, Eq. (10) may be solved to obtain the XEC ratios $2 \times S_1^{hkl} / \frac{1}{2}S_2^{200}$ and $\frac{1}{2}S_2^{111} / \frac{1}{2}S_2^{200}$.

It can be shown straightforwardly that it holds for the *apparent* Young's elastic modulus, E^{hkl}:

$$E^{hkl} = \frac{1}{S_1^{hkl} + \frac{1}{2}S_2^{hkl}} \quad (13)$$

Hence, the ratio of Young's moduli can be expressed in terms of the XEC ratios introduced above, as:

$$\frac{E^{200}}{E^{111}} = \frac{S_1^{111} + \frac{1}{2}S_2^{111}}{S_1^{200} + \frac{1}{2}S_2^{200}} = \frac{\frac{S_1^{111}}{\frac{1}{2}S_2^{200}} + \frac{\frac{1}{2}S_2^{111}}{\frac{1}{2}S_2^{200}}}{\frac{S_1^{200}}{\frac{1}{2}S_2^{200}} + 1} \quad (14)$$

Next, for each layer the narrow range of $a_{\varepsilon=0}$ and β values that yields physically self-consistent results, is determined by evaluating the calculated XEC ratios against the following physically motivated criteria:

i. $\frac{1}{2}S_2^{hkl} > 0$ (i.e. negative slopes of $\sin^2\psi$-plot for compressive stress).
ii. Elastic modulus $E^{hkl} = \frac{1}{S_1^{hkl} + 1/2S_2^{hkl}} > 0$.
iii. Poisson ratio $\nu^{hkl} = -S_1^{hkl} \cdot E^{hkl} \in [0;0.5]$.

Only results obtained for the upper eight layers fulfilled these criteria. The lack of self-consistent results for the lower layers is attributed to uncertainties in the experimentally determined slopes and intercepts combined with the ghost stresses at the transition from case to core. The $a_{\varepsilon=0}$ values fulfilling the above criteria coincide with the lattice parameter values derived from 111 Voigt and the 111 and 200 Reuss lattice spacings in Fig. 8(a), while the lattice parameters obtained from the 200 Voigt in Fig. 8(a) were generally not included. All stacking fault density values within the range 0–0.03 for the permitted $a_{\varepsilon=0}$ values met the set of criteria (i)–(iii).

The XEC and E-moduli ratios are presented as a function of $a_{\varepsilon=0}$ in Fig. 9. Note that each layer gives results for the permitted range of $a_{\varepsilon=0}$ values, i.e. a horizontal spread, while the vertical spread for each $a_{\varepsilon=0}$ value reflects the influence of variations in the stacking fault probability β. A fairly large scatter in horizontal and vertical directions occurs for the $2 \times S_1^{hkl} / \frac{1}{2}S_2^{200}$ ratios. Nevertheless the absolute change over the entire data range is relatively small. By contrast, the $\frac{1}{2}S_2^{111} / \frac{1}{2}S_2^{200}$ ratio shows a clear systematic change with the strain-free lattice parameter (=nitrogen content) and hardly any vertical scatter, indicating that the influence of stacking faults is small. Also, the ratio between the E-moduli increases systematically with nitrogen content and is fairly insensitive to stacking faults.

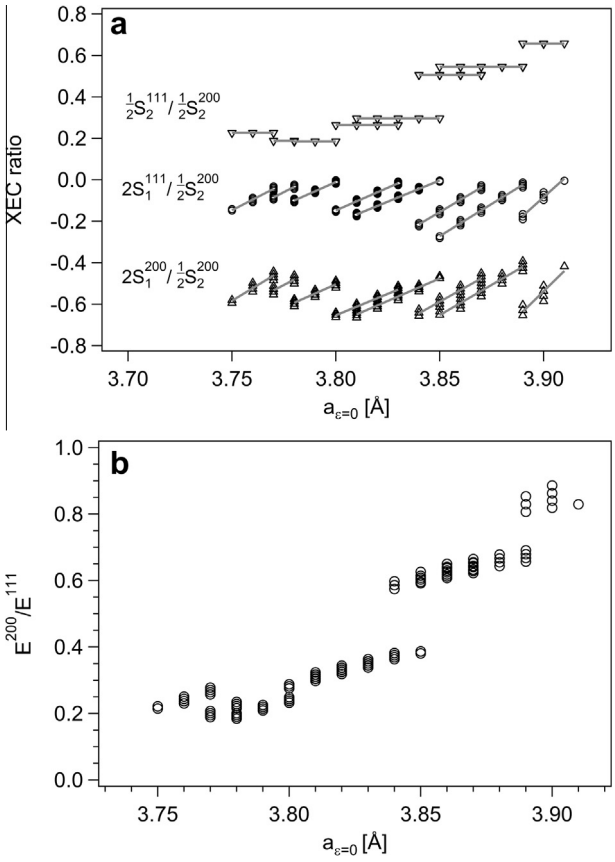

Fig. 9. XEC (a) and E-modulus ratios (b) as a function of the strain-free lattice parameter. Lines in (a) connect the range of results obtained from the same layer. Results from some of the layers overlap, in particularly in the plot of ratio of E-moduli.

The increase in E-modulus ratio with the nitrogen content is in qualitative agreement with a change of elastic anisotropy as concluded on the basis of nano-indentation measurements, where it was shown that for expanded austenite $E^{200} > E^{111}$ while for nitrogen-free austenite $E^{200} < E^{111}$ [8]. The *hkl* dependent Young's moduli of γ-Fe and γ′-Fe_4N (corresponding to $a_{\varepsilon=0} = 3.89$ Å [36] in Fig. 9(a)), as obtained by ab initio calculations [37] show a similar qualitative agreement: $\gamma : \frac{E^{200}}{E^{111}} = 0.33$ $\gamma' : \frac{E^{200}}{E^{111}} = 1.81$, which corresponds to an increase of this ratio by a factor 5.5. In comparison and regardless of the absolute values, in Fig. 9(a) an increase by a factor 4.5 is obtained for the same lattice parameter, indicating that, indeed, the elastic constants in expanded austenite depend strongly on the nitrogen content.

The presently obtained XECs are all relative to an unknown value of $\frac{1}{2}S_2^{200}$, which may also depend on the nitrogen content. For this reason the present results cannot be exploited to calculate absolute stress profiles. It is emphasised that the present calculations are not based on any assumptions concerning the GIM. The actual grain interaction mechanism is automatically included in the determined XEC ratios. This mechanism may be probed in more detail using the 3DXRD method based on synchrotron radiation to determine grain-resolved elastic strains [38].

5. Conclusions

The determination of residual stress by X-ray diffraction in nitrogen stabilised expanded austenite is not straightforward and complicated by the following conditions:

- The overlap of diffracted intensity from expanded austenite and the austenite substrate necessitates evaluation of the centroid rather than peak position in the transition zone. This leads to unreliable lattice strains in the transition zone from case to core, because non-linear $sin^2\psi$ dependencies arise.
- Steep gradients in the nitrogen concentration can lead to appreciable ghost stress effects, even for the application of grazing incidence X-ray diffraction with constant incidence angle. It was demonstrated that a variation in information depth from 0.35 μm to 0.18 μm over the applied tilt angle range can lead to ghost stresses exceeding 1 GPa. Generally, ghost stresses of about 200 MPa apply as a consequence of the concentration profile.
- Application of the Voigt and Reuss grain interaction models (GIM) does not result in upper and lower bound predictions of the stress, as expected. The use of XECs based on single crystal constants for nitrogen-free alloys has been identified as a major error source.
- The dependence of the XECs on the nitrogen content has been deduced from the experimental $sin^2\psi$ plots. A systematic increase in the $\frac{1}{2}S_2^{111}/\frac{1}{2}S_2^{200}$ ratio with the nitrogen concentration has been found as well as a corresponding increase in the ratio of apparent elastic moduli E^{200}/E^{111} by a factor 4.5.

Acknowledgments

Frederico A.P. Fernandes is grateful to the CNPq Brazilian council for the scholarship granted under the process number 201858/2011-8.

References

[1] B.H. Kolster, VDI-Berichte 506 (1983) 107–113.
[2] Z.L. Zhang, T. Bell, Surf. Eng. 1 (1985) 131–136.
[3] T.L. Christiansen, M.A.J. Somers, Int. J. Mater. Sci. 100 (2009) 1361–1377.
[4] H. Dong, Int. Mater. Rev. 55 (2010) 65–98.
[5] M.A.J. Somers, T.L. Christiansen, in: J. Dornett, G.E. Totten (Eds.), Heat Treatment of Iron and Steels, ASM Handbook, vol. 4D, 2014, pp. 439–450.
[6] T. Christiansen, M.A.J. Somers, Scr. Mater. 50 (2004) 35–37.
[7] T. Christiansen, M.A.J. Somers, Metall. Mater. Trans. A 37 (2006) 675–682.
[8] P. Villechaise, J.C. Stinville, C. Tromas, C. Templier, Scr. Mater. 64 (2011) 37–40.
[9] G. Abrasonis, A. Martinavicius, J.C. Stinville, P. Villechaise, C. Templier, P.O. Renault, et al., Surf. Coat. Technol. 204 (2010) 2551–2558.
[10] J.C. Stinville, C. Templier, J.P. Riviere, M. Drouet, P. Villechaise, Acta Mater. 58 (2010) 2814–2821.
[11] J.C. Stinville, J. Cormier, C. Templier, P. Villechaise, Acta Mater. 63 (2015) 10–16.
[12] B. Brink, K. Ståhl, T.L. Christiansen, M.A.J. Somers, J. Appl. Cryst. 47 (2014) 819–826.
[13] T. Christiansen, M.A.J. Somers, Mater. Sci. Eng. A 424 (2006) 181–189.
[14] S. Jegou, T.L. Christiansen, M. Klaus, Chr. Genzel, M.A.J. Somers, Thin Solid Films530, 2013, pp. 71–76.
[15] M.A.J. Somers, E.J. Mittemeijer, Metall. Mater. Trans. A 21 (1990) 189–204.
[16] T.L. Christiansen, M.A.J. Somers, Metall. Mater. Trans. A 40 (2009) 1791–1798.
[17] U. Welzel, J. Ligot, P. Lamparter, A.C. Vermeulen, E.J. Mittemeijer, J. Appl. Cryst. 38 (2005) 1–29.
[18] A. Kumar, U. Welzel, E.J. Mittemeijer, J. Appl. Phys. 100 (2006) 114904.
[19] T. Ersbacher, A. Wanner, T. Beck, O. Vöhringer, J. Appl. Cryst. 41 (2008) 377–385.
[20] W. Voigt, Lehrbuch der Kristallphysik, Teubner, Leipzig, 1910.
[21] A. Reuss, Z. Angew. Math. Mech. 9 (1929) 49–58.
[22] J.D. Eshelby, Proc. R. Soc. A 241 (1957) 376–396.
[23] E. Kröner, Z. Phys. 151 (1958) 504–508.
[24] R. Hill, Proc. R. Soc. 349 (1952) 349–354.
[25] H. Neerfeld, Mitt. K.-Wilh.-Inst. Eisenforschg. 24 (1942) 61–70.
[26] R.W. Vook, F. Witt, J. Appl. Phys. 36 (1965) 2169–2171.
[27] F. Witt, R.W. Vook, J. Appl. Phys. 39 (1968) 2773.
[28] U. Welzel, M. Leoni, E.J. Mittemeijer, Philos. Mag. 83 (2003) 603–630.
[29] A. Teklu, H. Ledbetter, S. Kim, L.A. Boatner, M. McGuire, V. Keppens, Metall. Mater. Trans. A 35 (2004) 3149–3154.
[30] T. Czerwiec, H. He, G. Marcos, T. Thiriet, S. Weber, H. Michel, Plasma Process. Polym. 6 (2009) 401–409.
[31] F. Bollenrath, V. Hauk, E. Müller, Z. Metallkd. 58 (1967) 76–82.
[32] F.A.P. Fernandes, T.L. Christiansen, M.A.J. Somers, Adv. Mater. Res. 996 (2014) 155–161.
[33] Residual Stress Measurement by X-ray Diffraction, Report No. SAE J784a, 2nd ed., SAE, Warrendale, PA, 1971.
[34] V. Hauk, R.W.M. Oudelhoven, G.J.H. Vaessen, Metall. Trans. 13A (1982) 1239–1244.
[35] B.E. Warren, X-ray Diffraction, Dover Publications Inc., New York, 1990 (chapter 13.5).
[36] M.A.J. Somers, N.M. van der Pers, D. Schalkoord, E.J. Mittemeijer, Metall. Trans. A 20 (1989) 1533–1539.
[37] T. Takahashi, J. Burghaus, D. Music, R. Dronskowski, J.M. Schneider, Acta Mater. 60 (2012) 2054–2060.
[38] J. Oddershede, S. Schmidt, H.F. Poulsen, L. Margulies, J. Wright, M. Moscicki, et al., Mater. Char. 62 (2011) 651–660.